



City Research Online

City, University of London Institutional Repository

Citation: Brokof, P., Guzmán-Iñigo, J., Yang, D. & Morgans, A. S. (2023). The acoustics of short circular holes with reattached bias flow. *Journal of Sound and Vibration*, 546(3), 117435. doi: 10.1016/j.jsv.2022.117435

This is the published version of the paper.

This version of the publication may differ from the final published version.

Permanent repository link: <https://openaccess.city.ac.uk/id/eprint/29306/>

Link to published version: <https://doi.org/10.1016/j.jsv.2022.117435>

Copyright: City Research Online aims to make research outputs of City, University of London available to a wider audience. Copyright and Moral Rights remain with the author(s) and/or copyright holders. URLs from City Research Online may be freely distributed and linked to.

Reuse: Copies of full items can be used for personal research or study, educational, or not-for-profit purposes without prior permission or charge. Provided that the authors, title and full bibliographic details are credited, a hyperlink and/or URL is given for the original metadata page and the content is not changed in any way.

City Research Online:

<http://openaccess.city.ac.uk/>

publications@city.ac.uk



The acoustics of short circular holes with reattached bias flow

Philipp Brokof^{a,*}, Juan Guzmán-Iñigo^{a,b}, Dong Yang^c, Aimee S. Morgans^a

^a Department of Mechanical Engineering, Imperial College London, London, UK

^b Department of Engineering, City University of London, Northampton Square, London EC1V 0HB, UK

^c Department of Mechanics and Aerospace Engineering, Southern University of Science and Technology, Shenzhen, 518055, PR China

ARTICLE INFO

MSC:

0000

1111

Keywords:

Hole acoustics

Vortex-sound interaction

LNSE

ABSTRACT

One of the most important parameters influencing the acoustic response of holes that sustain a low-Mach-number bias flow is their length-to-diameter ratio. For sufficiently short holes, the bias flow is detached within the hole's length, while in long holes the bias flow reattaches. The acoustic behaviour of each class is different and separate modelling approaches exist in the literature. For many technical applications, however, the length-to-diameter ratio falls in the range $1.5 < L_h/D_h < 3.0$, where it is not clear if the holes behave acoustically as short or long holes. In this work, the acoustics of such medium holes are explored numerically and analytically. The numerical approach is based on the linearisation of the compressible Navier–Stokes equations (LNSE) around a Reynolds-averaged mean flow. Medium holes are shown to whistle at higher Strouhal numbers than short holes although the mean flow reattaches within them. The underlying physics are further investigated by incorporating selected flow features of the LNSE results into a semi-analytical model accounting for vortex-sound interaction. It is shown that the perturbation field is determined by the three-way coupling of the two vortex sheets shed from the inlet and outlet edges of the hole with the acoustic field. Furthermore, the modelling of the growth of vorticity inside the hole is shown to be crucial to enable whistling in the semi-analytical model.

1. Introduction

Circular holes sustaining a low-Mach and high-Reynolds-number bias flow are found in many technical applications such as liquid rocket engine propellant injectors [1,2], acoustic liners [3] and Helmholtz resonators [4,5] in gas turbines. Such holes can either damp or generate acoustic energy [6,7], the latter being known as whistling. Their acoustic behaviour depends on a complex interplay between incident and scattered acoustic waves, and vorticity that is shed at the hole lips [8,9].

The length (thickness) of the hole determines different classes of holes by determining the mean flow topology inside them. Regardless of the hole length, the mean flow separates at the sharp hole inlet edge resulting in a low-speed recirculation zone close to the wall separated from the central jet by a thin shear layer. When the hole is short, the flow cannot reattach within the hole as shown in Fig. 1(a). In contrast, for longer holes, turbulent flow reattachment (caused by the high mean flow shear rates inside the hole [10]) takes place within the hole's length (Fig. 1(b)). Based on this difference in mean flow topology, conventional short and long holes can be defined, respectively. Lichtarowicz et al. [11] investigated experimentally the low-Mach-number, high-Reynolds-number and non-cavitating flow through long holes up to length-to-diameter ratios of 10. They found that, for length-to-diameter ratios $L_h/D_h < 1$, reattachment inside the hole is unlikely to occur [11]. To justify this, they reported the values of the discharge coefficient (defined as the ratio of the actual mass flow rate at the hole to that of an ideal nozzle) and argued that, for holes where

* Corresponding author.

E-mail address: philipp.brokof@tum.de (P. Brokof).

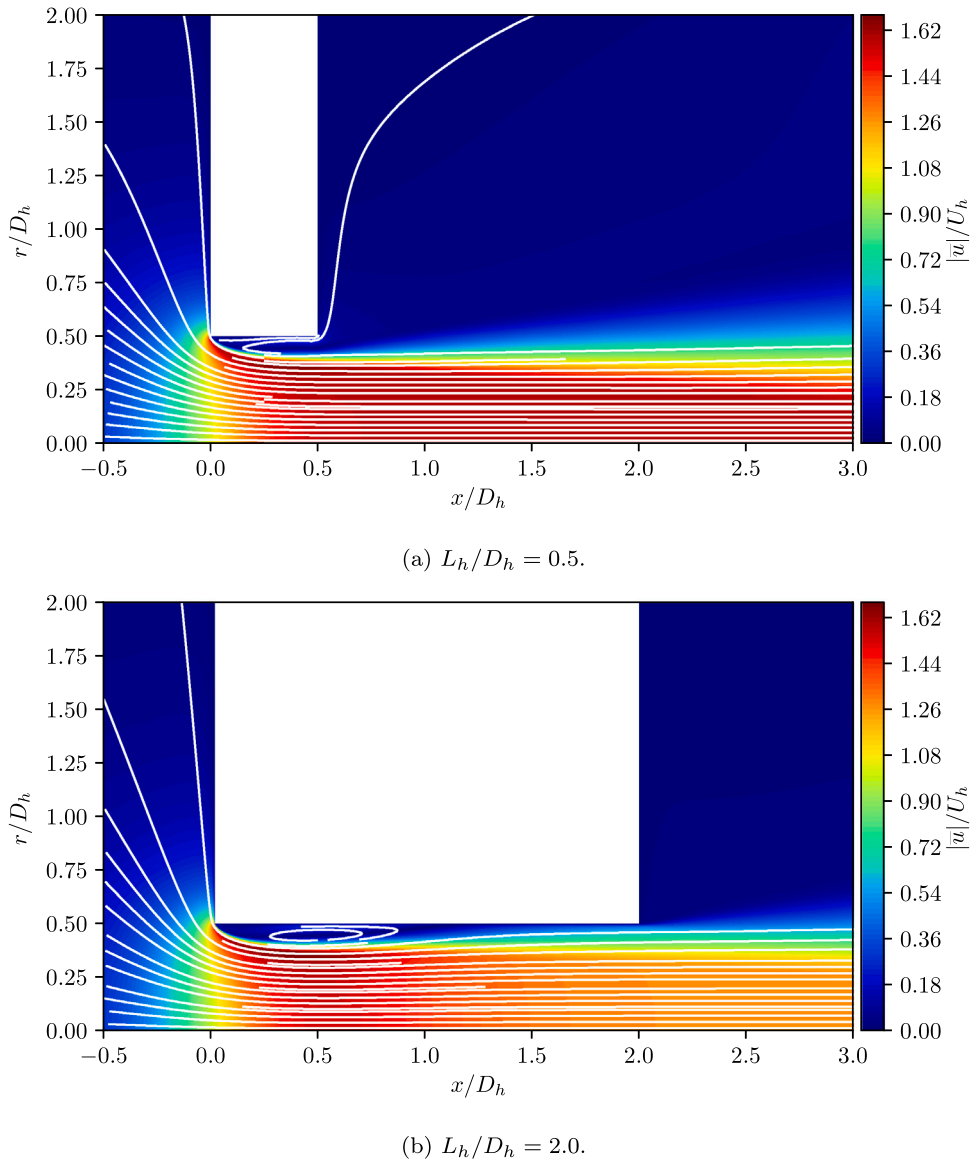


Fig. 1. Mean flow velocity magnitude and streamlines inside the hole. Velocities are normalised with the bulk velocity inside the hole. Detached flow in hole (a) and turbulent reattachment (b).

flow reattachment is not complete, this coefficient varies rapidly with the length of the hole [11,12]. This happens because, for short holes, the pressure drop is mainly produced by the reduction of the effective flow area (due to the presence of the separation) and the subsequent acceleration of the central jet. For short holes, the minimal effective flow area is strongly affected by the exact length and, hence, the strong variation of the discharge coefficient. In contrast, once the flow is fully reattached, the area at the vena contracta does not change significantly and, consequently, the discharge coefficient remains flatter (with a gentle decrease for increasing hole lengths due to turbulent friction losses). Lichtarowicz et al. [11] found that beyond a value of $L_h/D_h \approx 1.5$, the discharge coefficient is approximately constant. Hay and Spencer [12] report from experiments a stabilisation of the discharge coefficient at $L_h/D_h \approx 2.0$. Similarly, strong variation of the discharge coefficient up to $L_h/D_h \approx 2.0$ is found in Idelchik [13]. The empirical correlation of Kolodize and Van Winkle [14] shows stabilisation at $L/D \approx 1.6$. Based on these experimental studies, the border between short and long holes can be expected to fall within $1.5 < L_h/D_h < 2.0$. Rennels and Hudson [15], for instance, propose $L_h/D_h > 1.4$ as the lower limit for long holes.

The different mean flow topologies result in different acoustic behaviours exhibited by short and long holes. The damping of acoustic energy by apertures in infinitely thin walls was studied analytically by Howe [8]. Howe assumed that the Reynolds number was sufficiently high for the perturbation field to be taken as inviscid everywhere except in the vicinity of the separation line, where viscous effects need to be taken into account to avoid the geometric singularity predicted by inviscid theory. To this end, vorticity is

allowed to be shed from the rim of the hole in such quantities as to eliminate the singularity (via the Kutta condition). Subsequently, the vorticity is assumed to be convected without change by the mean flow along the shear layer. Howe modelled the thin regions of vorticity shed from the hole rim as a vortex sheet [16] and described the interplay between vorticity and the acoustic field. Yang and Morgans [9,17] extended Howe's model to account for the vortex-sound interaction inside short but finite holes. The straight vortex sheet shed from the hole in Howe's model, was replaced by a curved vortex sheet starting at the inlet edge of the hole and following the geometry of the vena contracta inside the hole. This model successfully describes the acoustic behaviour of short but finite holes. For a Strouhal number based on the hole length and the bulk velocity inside the hole, short holes ($L_h/D_h < 0.5$) are found to whistle in the range $0.2 < St < 0.35$ [7,18–22]. When whistling occurs, energy is transferred from the mean flow to the acoustic field through the unsteady vorticity shed at the sharp rims of the hole [9].

Longer holes with $L_h/D_h \in [5, 10]$ have been studied numerically [20] and experimentally [21] and no whistling was found. For long holes, the vorticity shed from the hole inlet is dissipated by turbulence before being convected to the hole outlet where it could interact with the radiated sound. Long holes were studied analytically based on Howe's model [8] by accounting for the hole length through an additional inertia term [3], or by allowing the propagation of planar acoustic waves inside the hole [9]. Bellucci et al. [4] developed a model for the acoustics of holes based on a momentum balance across the hole that needs the hole discharge coefficient as an input parameter.

Whereas the acoustics of short and long holes are well described by theoretical models, the border region between these two classes of holes, i.e. $1.0 < L_h/D_h < 5.0$, has been little investigated. Whistling of a hole with $L_h/D_h = 1.5$ is reported for $0.87 < St < 1.0$ [19,23], at significantly higher Strouhal numbers than the whistling range of conventional short holes. The existence of whistling for holes with a reattached mean flow in a different frequency range than for short holes suggests that the underlying physical mechanism of such holes must be different. In this work, the acoustics of holes with length-to-diameter ratios falling between $1.5 < L_h/D_h < 3.0$ are studied numerically and analytically. The lower boundary is chosen based on the observations by Lichtarowicz et al. [11] of stabilised discharge coefficient at $L_h/D_h > 1.5$, allowing to explore the so far unexplained whistling despite reattached hole flow. Length-to-diameter ratios smaller than 1.5 are excluded from the present study because the hole flow may be three-dimensional and hysteresis effects may occur [11].

The acoustics of the aforementioned holes are explored numerically to gain understanding of the underlying physics and to open the path to efficient analytical modelling. Numerical studies can be based on the Navier–Stokes equations with increasing contributions of modelling. The hole acoustics can be directly extracted from compressible time-resolved large eddy simulations (LES) which resolve large scale turbulent structures and account for non-linear effects [24,25]. To overcome the high demand of computational resources inherent to LES, the impedance of an acoustically compact hole was also extracted from Unsteady Reynolds-averaged Navier–Stokes (URANS) simulations [20,22,26]. While significantly reducing the computational effort by complete modelling of turbulence, this approach still accounts for the non-linear impact of the acoustics on the mean flow. Further reduction of the computational effort can be achieved by a two-step approach [27–29], i.e. solving the linearised Navier–Stokes equations (LNSE) for a mean flow that was obtained as the solution of the steady Reynolds-averaged Navier–Stokes equations (RANS). Inherently, this approach cannot account for non-linear effects and applies only to configurations that feature a time-averaged steady mean flow. To incorporate the influence of turbulence on the linear acoustics in the two-step approach, a turbulence model for the LNSE based on the mean flow eddy viscosity was proposed by Gikadi et al. [30] and Holmberg et al. [31].

The linear two-step approach with eddy viscosity is employed in this study for two reasons: (1) The high computational efficiency allows to perform a parametric study of the length-to-diameter ratio in the investigated border region between conventional short and long holes while obtaining the acoustic response of the holes over a broad frequency band. The latter is necessary, since the whistling of conventional short and medium holes occurs at low and high Strouhal numbers, respectively. (2) As for conventional short holes, a linear whistling mechanism is expected. Previous studies have shown the ability of LNSE to achieve excellent results for linear acoustic problems [27–31]. The choice of LNSE then allows the computational resources to be investigated in high mesh quality instead of resolving non-relevant flow details. This is especially important at higher frequencies. This can be observed, for instance, in the LES results of a hole ($L_h/D_h = 0.3$) given by Lacombe et al. [25], where the scattering matrix differs significantly from experimental trends at higher Strouhal numbers. The LNSE approach, in contrast, yields an excellent agreement over all frequencies for the same configuration, as we show in [Appendix A](#).

A further contribution of this paper is a semi-analytical model for the acoustics of holes in the aforementioned region. Yang and Morgans' [9,17] semi-analytical model is extended to account for the vorticity distribution identified by the LNSE approach for the holes of interest. This includes the three-way coupling of two vortex sheets with the acoustic field and the introduction of an additional model parameter to account for the growth of vorticity inside the hole at high Strouhal numbers.

This paper is organised as follows: Section 2 defines the problem studied in this paper in detail. Subsequently, the numerical and semi-analytical models employed in this paper are presented in Section 3.1 and Section 3.2, respectively. Section 4 presents and discusses the results of this study. The presented numerical approach is validated for low Strouhal numbers by comparison with experimental data in Section 4.1 and Section 4.2. In Section 4.3, the vorticity shed from the hole edges is analysed in the context of the vortex sound equation [16]. Key flow features enabling the whistling potential of this class of holes are identified in by incorporating them from the LNSE results into semi-analytical vortex-sound models [9,17,32] as shown in Section 4.4. This leads to the suggestion of the class of medium holes based on the underlying physical mechanism. Finally, the findings are summarised in Section 5.

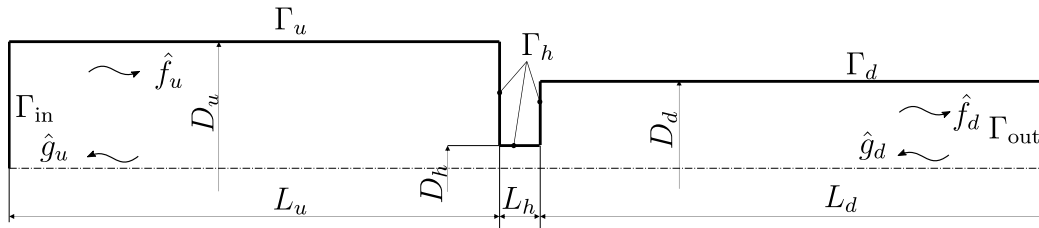


Fig. 2. Computational domain for acoustic characterisation of holes: Rotational symmetry around the duct axis is assumed. Boundaries are denoted with $\Gamma_{(\cdot)}$.

2. Problem formulation

A circular hole of diameter D_h and length L_h and arranged between two circular ducts is considered as shown in Fig. 2. Quantities upstream and downstream of the hole are denoted with the subscripts $(\cdot)_u$ and $(\cdot)_d$, respectively. Quantities considering the hole itself are denoted with the subscript $(\cdot)_h$. The geometry is determined by the up- and downstream expansion ratios $\lambda_u = D_u/D_h$ and $\lambda_d = D_d/D_h$, as well as the length-to-diameter ratio of the hole L_h/D_h . A uniform mean flow enters the domain at Γ_{in} , causing a bias flow through the hole. A small-amplitude acoustic wave coming from the upstream side is then imposed on this mean flow. We formulate the problem in the frequency domain by choosing the ansatz $\tilde{(\cdot)} = \hat{(\cdot)} \exp(i\omega t)$ for small perturbations, where t is the time and i the imaginary unit. As the considered frequencies $\omega = 2\pi f$ are below the cut-off frequency of the ducts, only acoustic plane waves are non-evanescent. The ducts in Fig. 2 are chosen to be sufficiently long ($L_u = 150D_h$, $L_d = 300D_h$), so that only one-dimensional planar acoustic waves propagate far up- and downstream from the hole. For comparability with other studies, frequencies are presented in non-dimensional form using the Strouhal number

$$St = \frac{f L_h}{U_h}, \tag{1}$$

based on the hole length and the mean bulk velocity inside the hole U_h .

Representative for holes with length-to-diameter ratios falling in between conventional short and long holes, a hole with $L_h/D_h = 2.0$ is chosen. The Mach number inside the hole, based on the hole bulk velocity U_h and mean flow speed of sound \bar{c} , is set to $Ma_h = U_h/\bar{c} = 0.043$ for comparison with available experimental data. The mean flow Mach number inside the hole is small which allows the mean flow to be modelled as incompressible. The Reynolds number inside the hole, based on the bulk velocity, hole diameter D_h and kinematic viscosity ν , is set to $Re_h = U_h D_h/\nu = 10,000$ throughout the paper. This is sufficiently high for the mean flow topology inside the hole to become independent of the Reynolds number [8,12].

A quantitative measure of the acoustic behaviour of the hole is its impedance

$$\mathcal{Z}_h = \frac{\Delta \hat{p}_h}{A_h \hat{u}_h}, \tag{2}$$

where $\Delta \hat{p}_h$ is the difference in acoustic pressure across the hole, A_h is the hole cross section area and \hat{u}_h is the axial acoustic velocity at the inlet of the hole. If the real part of the impedance, known as the resistance, becomes negative, the hole generates acoustic energy [8,33]. For comparison with other studies, the impedance is given in its normalised form

$$Z_h = \frac{A_h}{\bar{\rho} \bar{c}} \mathcal{Z}_h = \frac{1}{\bar{\rho} \bar{c}} \frac{\Delta \hat{p}_h}{\hat{u}_h}, \tag{3}$$

assuming a constant mean flow density $\bar{\rho}$ and speed of sound \bar{c} .

3. Models and their assumptions

In this section, we describe the numerical (Section 3.1) and analytical (Section 3.2) models that we use to study the configuration outlined in Section 2. Furthermore, we outline the underlying assumptions of each model.

3.1. Numerical model

In this work, the mean flow Mach number is assumed to be low. Hence, the mean flow through the hole can be assumed incompressible and entropy fluctuation can be neglected [27–29]. The problem is, therefore, completely governed by the conservation of mass and momentum,

$$\frac{\partial \rho}{\partial t} + \nabla \cdot (\rho \mathbf{u}) = 0, \tag{4}$$

$$\frac{\partial (\rho \mathbf{u})}{\partial t} + \nabla \cdot (\rho \mathbf{u} \otimes \mathbf{u}) = -\nabla p + \nabla \cdot \underline{\underline{\tau}}, \tag{5}$$

where ρ is the density, p is the pressure and \mathbf{u} is the velocity. Body forces are neglected in this formulation. For the assumed Newtonian fluid, the shear stress tensor is defined as

$$\underline{\underline{\tau}} = \eta \underline{\underline{\epsilon}} = \eta \left[(\nabla \mathbf{u} + \nabla \mathbf{u}^T) - \frac{2}{3} (\nabla \cdot \mathbf{u}) \underline{\underline{\mathbf{I}}} \right], \tag{6}$$

where η is the dynamic viscosity and $\underline{\underline{\epsilon}}$ is the shear rate tensor. The unit tensor is denoted by $\underline{\underline{\mathbf{I}}}$.

To model the influence of turbulence on the linear acoustics, the Navier–Stokes equations are Reynolds-averaged [34]. To this purpose, primitive flow variables $\mathbf{Y} = (\mathbf{u}, \rho, p)$ are decomposed into a steady mean flow $\bar{\mathbf{Y}}$, small-amplitude, coherent oscillations $\tilde{\mathbf{Y}}$ and small random turbulent fluctuations \mathbf{Y}' , such as

$$\mathbf{Y} = \bar{\mathbf{Y}} + \tilde{\mathbf{Y}} + \mathbf{Y}'. \tag{7}$$

This triple decomposition is introduced in Eq. (4) and Eq. (5) and the time average is taken. After neglecting second-order terms of the coherent oscillations, the Reynolds-averaged Navier–Stokes (RANS) equations are obtained for the mean flow. Here, the RANS equations are solved with the finite volume software OpenFoam version 7.0 [35], using a segregated solver based on the SIMPLE algorithm. Turbulence is modelled with the $k - \omega$ -SST turbulence model [36], which can treat wall-bounded and free-shear flows simultaneously [36–38]. This property is necessary since flow separation inside the hole and a shear layer convected downstream from the hole are present in the mean flow.

Exploiting the rotational symmetry of the problem, the structured mean flow mesh is a 5 degree wedge composed of hexahedral cells with a row of prismatic cells around the axis of revolution. This mesh extends only one layer in the circumferential direction with boundary conditions in the two bounding planes that ensure axisymmetry of the flow variables. The duct wall upstream of the hole Γ_u is treated with a slip boundary condition $\bar{\mathbf{u}} \cdot \mathbf{n} = 0$ since it models a plenum. The wall containing the hole Γ_h , as well as the downstream duct wall Γ_d , are treated with a non-slip boundary condition $\bar{\mathbf{u}} = 0$ to capture the influence of the recirculating flow, due to the area expansion, on the acoustics. In a parametric study, the expansion ratio $\lambda = D_d/D_h$ is increased until independence of the acoustic results on the expansion ratio is found. At no-slip walls, the mesh resolves the boundary layer with a dimensionless wall distance of $y^+ < 1$ to avoid the use of wall functions for the turbulence modelling. A uniform velocity profile is set at the inlet Γ_{in} to yield a mean velocity of $U_h = 1$ inside the hole. Additionally, the turbulent kinetic energy at the inlet is imposed so that a turbulence intensity of 5% is achieved. The viscosity is adjusted to match the target Reynolds number inside the hole. Zero gradients are set for the pressure and specific dissipation rate of turbulent kinetic energy on the inlet. The flow leaves the computational domain at prescribed zero relative pressure and the gradients of velocity, specific dissipation rate of turbulent kinetic energy and turbulent kinetic energy are set to zero at the outlet Γ_{out} .

The governing equations for perturbations of the mean flow are obtained by inserting the triple decomposition (Eq. (7)) into Eqs. (4) and (5), and subsequent subtraction of the time-averaged $\bar{\cdot}$ equations from the phase-averaged $\langle \cdot \rangle$ ones. By neglecting perturbation terms of order two and higher, we find the linearised Navier–Stokes equations (LNSE) as

$$\frac{\partial \bar{p}}{\partial t} + \nabla \cdot (\bar{\rho} \bar{\mathbf{u}} + \bar{p} \bar{\mathbf{u}}) = 0, \tag{8}$$

$$\frac{\partial \bar{\rho} \bar{\mathbf{u}}}{\partial t} + (\bar{\rho} \bar{\mathbf{u}} + \bar{p} \bar{\mathbf{u}}) \cdot \nabla \bar{\mathbf{u}} = \nabla \cdot \left(\underline{\underline{\tau}} - \bar{\rho} \langle \mathbf{u}' \otimes \mathbf{u}' \rangle - \overline{\mathbf{u}' \otimes \mathbf{u}'} \right) - \nabla \bar{p}. \tag{9}$$

For a detailed derivation, the reader is referred to Gikadi et al. [30] and Holmberg et al. [31]. When entropy perturbations are neglected, the equation of state reduces to $\bar{p} = \bar{\rho} \bar{c}^2$. Turbulence is modelled by relating the time and phase-averages of double-correlations of turbulent fluctuations in Eq. (9) to the harmonic perturbation strain rate tensor with the Boussinesq hypothesis [30,31]

$$\langle \mathbf{u}' \otimes \mathbf{u}' \rangle - \overline{\mathbf{u}' \otimes \mathbf{u}'} = \left[-\nu_T \langle \underline{\underline{\epsilon}} \rangle + \frac{2}{3} \langle k \rangle \underline{\underline{\mathbf{I}}} \right] + \left[\nu_T \bar{\underline{\underline{\epsilon}}} - \frac{2}{3} k \underline{\underline{\mathbf{I}}} \right] = -\nu_T \bar{\underline{\underline{\epsilon}}}. \tag{10}$$

Eq. (10) assumes that the energy of the turbulence k is not affected by phase averaging and therefore, cancels out. Furthermore, the property of phase and time-averaging, $\bar{\underline{\underline{\epsilon}}} = \langle \underline{\underline{\epsilon}} \rangle - \bar{\underline{\underline{\epsilon}}}$, is used. We further assume that the turbulence is unaffected by the acoustic perturbation [39] and, hence, the eddy viscosity $\eta_T = \bar{\rho} \nu_T$ is assumed “frozen” and equal to the one obtained from the mean flow solution. Finally, Eqs. (8) and (9) are transformed to the frequency domain by using the ansatz $\tilde{\mathbf{Y}} = \hat{\mathbf{Y}} e^{i\omega t}$ for harmonic perturbations. These equations are solved within the finite element framework FEniCS [40] using a coupled approach [39].

As for the mean flow computations, the rotational symmetry of the problem is exploited in the acoustic simulations. The governing equations are formulated in cylindrical coordinates and an unstructured two-dimensional mesh consisting of triangular elements is used. Anechoic acoustic boundary conditions based on a flux vector splitting approach (Appendix B) are set at the domain inlet Γ_{in} and outlet Γ_{out} . The flow is acoustically forced from the inlet. For the acoustics, the upstream duct wall Γ_u is again modelled with a slip boundary condition $\hat{\mathbf{u}} \cdot \mathbf{n} = 0$ since its purpose is to model a plenum where viscous losses are negligible. The wall containing the hole Γ_h is treated with a non-slip boundary condition $\hat{\mathbf{u}} = 0$. In the acoustic simulations, the downstream duct wall is also modelled with a slip boundary condition $\hat{\mathbf{u}} \cdot \mathbf{n} = 0$ to reduce the computational cost associated with solving the acoustic boundary layer. Comparative studies between simulations with acoustic no-slip and slip boundary conditions at the downstream duct wall showed only a small influence on the results. Additionally, Kierkegaard et al. [28] report that a high resolution of the acoustic boundary layer is not necessary to obtain reliable results. For a hole Mach number of $Ma_h = 0.043$ and a maximum Strouhal number of $St = 1.2$, the shortest acoustic wave length at the coarsest part of the mesh in the upstream duct is $\lambda/L_h \approx 19.4$. This yields a resolution of approximately 55 elements per wavelength.

The Riemann invariants, which represent the amplitude and phase of plane acoustic waves propagating in and opposite to the flow direction, are defined as

$$\hat{f} = \frac{1}{2} \left(\frac{\hat{p}}{\hat{\rho}\hat{c}} + \hat{u} \right), \quad \hat{g} = \frac{1}{2} \left(\frac{\hat{p}}{\hat{\rho}\hat{c}} - \hat{u} \right), \quad (11)$$

respectively, and are extracted from the LNSE results with a numerical analogue of the multiple-microphone method [41]. The two post-processing zones are $-100 < x/D_h < -10$ upstream and $40 < x/D_h < 100$ downstream of the hole outlet. Under the assumption of local incompressibility at the hole, the pressure difference across the hole is the pressure difference between the up- and downstream ducts at the duct-hole-interfaces

$$\frac{\Delta\hat{p}_h}{\hat{\rho}\hat{c}} = (\hat{f}_u + \hat{g}_u) - (\hat{f}_d + \hat{g}_d), \quad (12)$$

and the velocity in the hole can be approximated from the velocity in the upstream duct

$$\hat{u}_h = \frac{A_u}{A_h} (\hat{f}_u - \hat{g}_u). \quad (13)$$

Both quantities together allow to compute the hole impedance Eq. (3).

To sum up, the most important assumptions of the numerical model are (1) incompressibility and steadiness of the mean flow, (2) the neglect of entropy fluctuations and (3) no influence of acoustic perturbations on the turbulence ("frozen eddy viscosity").

3.2. Semi-analytical model

We now turn our attention to the theoretical description of the problem. The presented semi-analytical model is based on the vortex-sound theory [8,9] and an extension of the model of Yang and Morgans [9,17] developed for short holes.

We consider flows characterised by low-Mach, $\mathcal{O}(Ma^2) \ll 1$, and high-Reynolds numbers $\mathcal{O}(Re_h) = 10^4 - 10^5$. The first limit allows to assume that entropy perturbations are negligible. The second limit allows to treat the perturbation field as inviscid. Viscous effects are only important close to the sharp edges of the hole, where viscosity produces the shedding of fluctuating vorticity when acoustic waves impinge them. In the model, the strength of the unsteady shed vorticity is chosen according to a Kutta condition [8], i.e. so that the perturbation velocity and pressure at the hole edges stay finite. The shed vorticity is then convected by the mean flow and, if viscous diffusion is neglected, it can be assumed to be contained in an infinitely thin region. This is known as the vortex sheet assumption [16] and has been extensively used to successfully model the acoustics of this type of flow, for example by Pedergnana et al. [42].

The flow through the hole is described in terms of the stagnation enthalpy $B = c_p T + \frac{1}{2} \mathbf{u}^2$, where c_p is the isobaric specific heat and T the temperature. In an irrotational low-Mach-number flow, the perturbed stagnation enthalpy \tilde{B} is linked to the acoustic pressure and acoustic velocity by $\tilde{p} = \tilde{\rho}(\tilde{B} - \tilde{u}\tilde{u})$ and $\frac{\partial \tilde{u}}{\partial t} = -\nabla \tilde{B}$, respectively [16]. Flow variables are represented as the sum of a steady mean component ($\bar{\cdot}$) and a small-amplitude perturbation component ($\tilde{\cdot}$). Neglecting body forces and assuming the flow to be homentropic with constant mean density and speed of sound, the distribution of the perturbation stagnation enthalpy \tilde{B} is governed by the following inhomogeneous wave equation [16],

$$\left(\frac{1}{\hat{c}^2} \left(\frac{\partial^2}{\partial t^2} + \bar{u} \frac{\partial}{\partial x} \right) - \nabla^2 \right) \tilde{B} = \nabla \cdot (\tilde{\xi} \times \bar{\mathbf{u}}), \quad (14)$$

where $\tilde{\xi}$ is the perturbation vorticity. To model this vorticity, we assume that the strength and phase of the vorticity shed at a given edge σ are determined by a Kutta condition and the vorticity is then advected with uniform convection velocity \mathbf{u}_c along the vortex sheet path, s , i.e.

$$\tilde{\xi} = \tilde{\xi} \mathbf{e}_\theta = \sigma e^{ik_0 s} \mathbf{e}_\theta, \quad (15)$$

where $k_0 = \omega/|\mathbf{u}_c|$ is the hydrodynamic wavenumber and \mathbf{e}_θ the unit vector in the azimuthal direction. In the rest of this paper, the mean velocity in the source term of Eq. (14) is replaced by the convective velocity associated with the vortex sheet.

If the walls with which the vortex sound interacts are not penetrated by the perturbation vorticity, the perturbed stagnation enthalpy must obey the potential flow wall boundary condition of vanishing normal velocity, $\tilde{\mathbf{u}} \cdot \mathbf{n} = 0$. The irrotational relation between acoustic velocity and perturbation total enthalpy allows to formulate this condition as

$$\frac{\partial \tilde{B}}{\partial \mathbf{n}} = 0. \quad (16)$$

In order to solve Eq. (14) the Green's function method is used [9,16,17,32]. The Green's function G is defined as the solution generated by a Dirac impulse δ at position \mathbf{y} and time τ :

$$\left(\frac{1}{\hat{c}^2} \left(\frac{\partial^2}{\partial t^2} + \bar{u} \frac{\partial}{\partial x} \right) - \nabla^2 \right) G = \delta(\mathbf{x} - \mathbf{y})\delta(t - \tau). \quad (17)$$

Eq. (14) can then be weighted by this Green's function and integrated over the physical domain. After some manipulations, the following integral solution for the stagnation enthalpy in the frequency domain [9,17] is obtained

$$\tilde{B}(x, \omega) = \int_S \left(2ik \overline{Ma} \hat{G} \tilde{B} \mathbf{e}_x + \hat{G} \nabla \tilde{B} - \tilde{B} \nabla \hat{G} \right) \cdot \mathbf{s} - \int_V (\tilde{\xi} \times \mathbf{u}_c) \cdot \nabla \hat{G} dv, \quad (18)$$

where k is the acoustic wavenumber and \mathbf{e}_x the unit vector in the axial direction. Note that to obtain a closed-form integral solution of Eq. (14), the Green's function is required to satisfy the boundary condition $\frac{\partial G}{\partial n} = 0$ on the wall boundaries.

To sum up, the most important assumptions of the semi-analytical model are (1) the neglect of entropy fluctuations, (2) the neglect of viscosity but in the vicinity of the sharp hole edges and (3) uniform convection of the shed vorticity.

4. Results and discussion

In this section, we present the results of our numerical study. Subsequently, the semi-analytical model described in Section 3.2 is extended by certain flow features obtained from the numerical results to improve its predictions. Based on the presented findings, we introduce the medium hole as new class of perforation with its own characteristic acoustical behaviour.

4.1. Mean flow as obtained by numerical model

Fig. 1(b) shows the velocity field for a hole defined by $L_h/D_h = 2.0$. The flow cannot follow the sharp geometry of the hole at the inlet and separates creating a low-speed recirculation region adjacent to the wall. A jet is created in the central zone of the hole. The thickness of the recirculation zone rapidly increases downstream of the inlet up to a vena contracta located at a distance of $x/D_h \approx 0.5$ from the inlet. In this portion, the velocity of the jet increases due to the reduction of the effective flow area produced by the presence of the separation. This increase of velocity however comes at the expense of a pressure drop. Downstream of the vena contracta, turbulence enhances the transfer of momentum between the boundary layer and the jet, leading to a turbulent reattachment of the flow at $x/D_h = 1.22$ (based on the change of sign of the wall friction coefficient). This value compares favourably with the reattachment line at $x/D_h = 1.15$ reported by Son et al. [43] for a hole with $L_h/D_h = 1.5$ using LES. With the increase of effective flow area downstream of the vena contracta, the velocity of the jet reduces and the pressure is recovered. Deckker and Chang [44] reports the pressure measured experimentally at the centre-line for a hole with $L_h/D_h = 2.0$. They found a minimum of the pressure (corresponding to the position of the vena contracta) at $x/D_h \approx 0.5$, in agreement with Fig. 1(b).

To compare the numerical results with experimental data, we use the loss coefficient defined as

$$\zeta = \frac{\Delta \bar{p}}{\frac{1}{2} \bar{\rho} U_h^2}, \quad (19)$$

where the $\Delta \bar{p}$ is the pressure difference between the inlet and the outlet of the domain. The loss coefficient quantifies the pressure loss across the domain, in this case, the pressure loss across the hole and any friction losses produced in the downstream duct. In the upstream duct, there are no viscous losses since a slip boundary is imposed at the wall. For holes up to $L_h/D_h < 2.0$, the wall friction inside the hole is negligible [11] and the pressure loss is mainly due to the contraction of the jet inside the hole. From the experimental data given by Idelchik [13], the loss coefficient of a hole with $L_h/D_h = 2.0$ can be computed as $\zeta = 1.55$. The empirical correlation of Rennels and Hudson [13] yields a loss coefficient of $\zeta = 1.566$. The loss coefficient obtained from the RANS is $\zeta = 1.6$, marking a relative difference of 3.13% and 2.13%, respectively.

Experimental values of the discharge coefficient C_d for similar holes are found in the literature and can be used to further quantify the quality of the simulations. The discharge coefficient is defined as the ratio of the actual mass flow rate at the hole to that of an ideal nozzle and is related to the loss coefficient as $C_d = 1/\sqrt{\zeta}$. Lichtarowicz et al. [11] report experimental values of the discharge coefficient in the range $C_d \approx 0.8 - 0.82$, and propose an empirical relation that yields $C_d = 0.8057$ for the parameters considered here. The discharge coefficient obtained from the RANS is $C_d = 0.79$ yielding a relative error of 1.88%. This difference could be partially explained by the different position of the pressure measurements: the pressure is measured at the inlet and outlet in the simulations, while corner tapings are used in the experiments. The small relative error between experimental/numerical data shows that the mean flow topology inside the hole is correctly captured, giving us confidence in the accuracy of the RANS predictions closed with the $k - \omega$ -SST turbulence model.

4.2. Impedance as obtained by numerical model

Fig. 3 shows the real Z_R and imaginary Z_I part of the normalised impedance for a hole with $L_h/D_h = 2.0$. For Strouhal numbers below 0.9, the LNSE results are insensitive to the expansion ratio. This is in agreement with results presented by Yang and Morgans [17] which indicate that the impedance converges to the plenum result for expansion ratios $\lambda = D_u/D_h = D_d/D_h \geq 5$ for short holes. In the low Strouhal number regime for which experimental data is available, the agreement between LNSE and experiment is good. The LNSE results predict a negative resistance for $St \gtrsim 0.8$, indicating a whistling potential of the hole.

Fig. 4 compares the impedance results obtained by the LNSE approach for increasing L_h/D_h ratios. The short hole with $L_h/D_h = 0.5$ whistles at $St \approx 0.25$. For such short holes, the whistling regime is reported to collapse in the range $0.2 < St < 0.35$ [23]. The introduction of the class of medium holes is motivated by the collapse of the whistling regimes of holes with L_h/D_h ratios of 1.5 and 2.0 at $0.8 < St < 1.1$ instead. This means that medium holes whistle at a three times higher Stouhal number than short holes, suggesting a different underlying whistling mechanism. Moussou et al. [19] report from experiments that a hole with $L_h/D_h = 1.5$ sustaining a mean flow with $Ma_h = 0.01$ can generate acoustic energy at $St \approx 1.0$. The experimental results also indicate that the whistling regime shifts to lower Strouhal numbers if the Mach number is increased. Testud [23] reports whistling at $St \approx 0.87$ for a similar hole with $Ma_h = 0.1$. If the hole length is further increased to L_h/D_h ratios of 2.5 and 3.0, the whistling potential of the

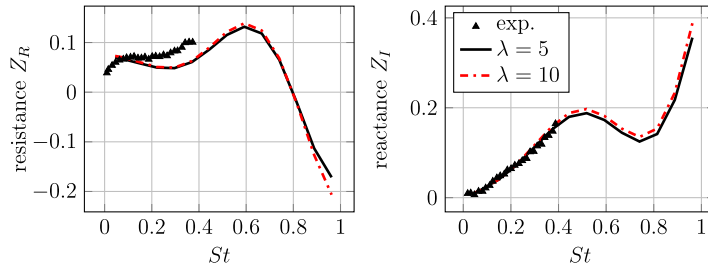


Fig. 3. Normalised impedance Z for a hole with $L_h/D_h = 2.0$ for different expansion ratios λ . Comparison with experimental data [21].

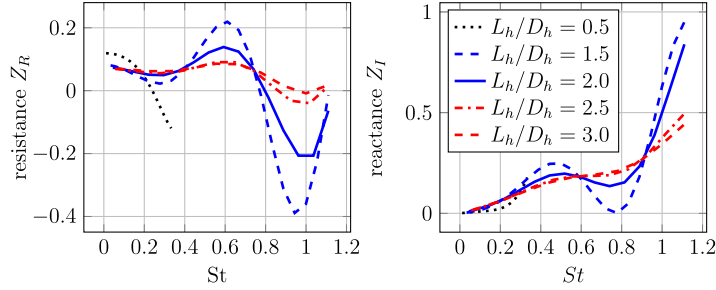


Fig. 4. Comparison of the normalised impedances of a short hole (black), medium holes (blue) and long holes (red). All computations were conducted with an expansion ratio of $\lambda = 10$. (For interpretation of the references to colour in this figure legend, the reader is referred to the web version of this article.)

hole in the higher Strouhal number regime begins to vanish. This is in agreement with findings in the literature that longer holes cannot whistle [20,21].

The whistling frequency range observed experimentally [19,23] for a hole with $L_h/D_h = 1.5$ agrees with the LNSE prediction of negative resistance at $0.75 < St < 1.1$ as shown in Fig. 4. In this paper, this phenomenon is referred to as the whistling of medium holes and is further investigated. Medium holes are long in the sense that the mean flow reattaches inside them but differ from conventional long holes by their whistling potentiality.

4.3. Analysis of the perturbation vorticity distribution

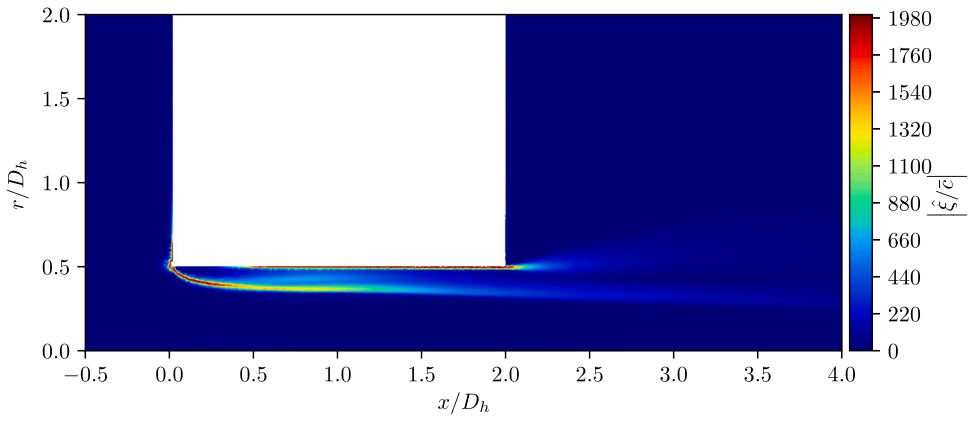
Eq. (18) illustrates that the knowledge of the distribution of the perturbation vorticity shed from the hole and its convection velocity are crucial to understand the acoustics of a medium hole.

Fig. 5 shows the distribution of perturbation vorticity ξ for a medium hole as obtained from the LNSE. We observe that, for the two frequencies, vorticity is shed from both the upstream and downstream edges, and is convected downstream in two thin regions. These regions will be modelled using the vortex sheet assumption as sketched in Fig. 6. The vorticity shed from the inlet edge, σ_1 , is first convected in the region that separates the recirculation bubble from the central jet and then, follows a straight path until it leaves the hole. We model this region with a vortex sheet whose shape is given by the ansatz [9]

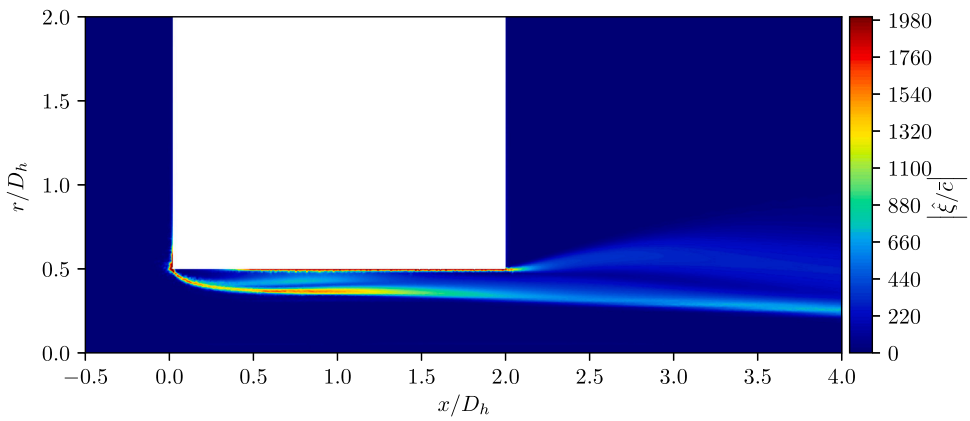
$$\frac{R_v}{R_h} = 1 - a(1 - e^{-b \frac{x}{R_h}}), \tag{20}$$

where R_v is the radius of the vortex sheet. From the contraction ratio of the vortex sheet in the LNSE, $a = 0.33$ is found, and $b = 6$ is chosen as in Yang and Morgans [9] for conventional short holes. Downstream of the hole, σ_1 is assumed to be parallel to the hole axis. The vorticity shed from the downstream edge leaves the edge parallel to the hole and is quickly diffused due to the strong turbulence. This second vortex sheet, σ_2 , is taken to be straight and parallel to the hole axis.

To investigate the importance of each vortex sheet on the acoustic response of the hole, models (1) to (3) in Fig. 6 are considered here. Model (4) in Fig. 6 is discussed later. The first and second model consider separately vorticity of constant strength shed from the upstream σ_1 and downstream σ_2 edges, respectively. The third model includes both vortex sheets of constant strength σ_1 and σ_2 and, thus, solves two Kutta conditions. The extension of the single vortex sheet model of [9,17,37] as presented in Section 3.2 for two vortex sheets is explained in Su et al. [32]. Fig. 7 compares the normalised impedance obtained with the three semi-analytical models for a hole with $L_h/D_h = 2.0$. For all three models, the convective speeds of the vortex sheets σ_1 and σ_2 were set to the bulk velocity U_h inside the hole. The model including only σ_1 does not match the LNSE trends of resistance or reactance. Instead, negative resistance at $0.3 < St < 0.6$, close to the conventional whistling range of short holes, is predicted. This is to be expected since the model captures the physics of the whistling mechanism of short holes. The model including only σ_2 predicts a constant resistance and linear increase of reactance with the Strouhal number. Thus, it does not capture the LNSE trends of the impedance of medium holes. Instead, this behaviour is typical for conventional long holes that cannot whistle. The model accounting for σ_1 and



(a) $St = 0.3$: Positive resistance.



(b) $St = 0.82$: Negative resistance.

Fig. 5. Magnitude of the normalised perturbation vorticity for $L_h/D_h = 2.0$.

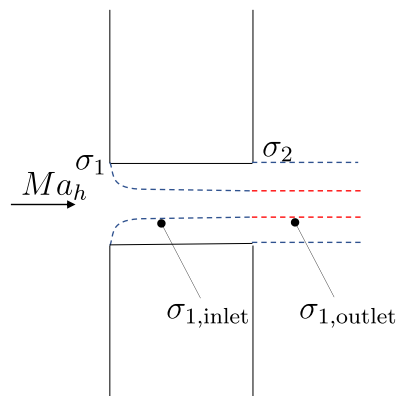


Fig. 6. Vortex sheet models for medium holes: (1) only σ_1 with constant strength, (2) only σ_2 , (3) σ_1 with constant strength and σ_2 , (4) σ_1 with jump in strength and σ_2 .

σ_2 qualitatively captures the overall trend of the resistance of the numerical simulations. A maximum and minimum in resistance at $St \approx 0.45$ and $St \approx 0.9$ are predicted. However, the quantitative match between LNSE and model is unsatisfactory. The resistance stays positive at higher Strouhal numbers so that whistling is not predicted by the model. The model also matches the LNSE trends

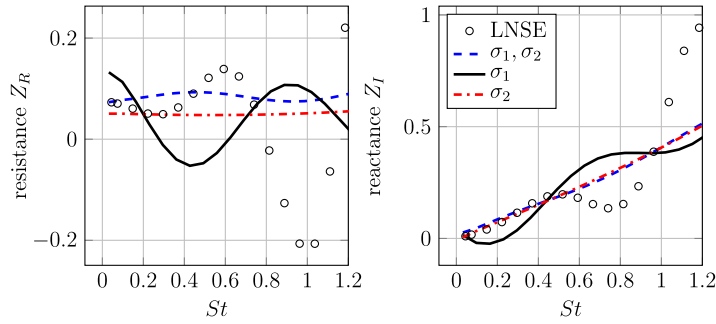


Fig. 7. Normalised impedance Z for a hole with $L_h/D_h = 2.0$ obtained with the vortex sheet model with only one vortex sheet shed from the inlet edge (σ_1), only one vortex sheet shed from the outlet edge (σ_2) and both vortex sheets (σ_1, σ_2). Results are compared with the LNSE data. The convection velocities in all models are set to the bulk velocity inside the hole.

Table 1
Normalised convection velocities u_c/\bar{c} of vortex sheets convected from the inlet edge (σ_1) and outlet edge (σ_2).

St	$u_{c,1}$	$u_{c,2}$
0.30	0.0359	0.0224
0.60	0.0309	0.0288
0.82	0.0367	0.0301

in reactance by showing an inflexion point at $St \approx 0.4$. However, as for the resistance, the quantitative match between model and LNSE in reactance is unsatisfactory.

4.4. Extraction of physical model parameters

We now seek to improve the quantitative match between the semi-analytical model and the simulations by extracting model parameters from the numerical simulations, i.e. the convection velocities associated to the vortex sheets and the vortex sheet strengths.

4.4.1. Convection velocity

Two model parameters according to Eq. (18) are the convection velocities $u_{c,1}$ and $u_{c,2}$ of the two vortex sheets σ_1 and σ_2 . The convection velocity of a vortex sheet can be estimated by tracking vorticity structures in the frequency domain [32]. This allows to identify a hydrodynamic wavelength λ_{hy} which when multiplied with the frequency f gives the convection velocity $u_c = \lambda_{hy}f$. Fig. 8 illustrates this using the real part of the normalised perturbation vorticity $\text{Re}(\hat{\xi}/\bar{c})$ for $St = 0.82$. Vorticity structures convected from the inlet and outlet edge can be identified. By connecting the minima and maxima of each structure, the total length of the trajectory L_t is obtained. The average wavelength can then be computed by dividing through the number of cycles N along the trajectory. This yields for the normalised convection velocity,

$$\frac{u_c}{\bar{c}} = \frac{L_t}{L_h} \frac{StMa_h}{N}. \tag{21}$$

Table 1 summarises the convection velocities obtained with Eq. (21) for different Strouhal numbers. The convection velocities averaged over the considered Strouhal numbers for σ_1 and σ_2 are $u_{c,1}/\bar{c} = 0.0345$ and $u_{c,2}/\bar{c} = 0.0271$. With absolute mean deviations of 0.0024 and 0.0031 for σ_1 and σ_2 , respectively, a constant average convection velocity for all Strouhal numbers is assumed.

The Mach number inside the hole, $Ma_h = U_h/\bar{c} = 0.043$, is the bulk velocity normalised with the speed of sound. For short holes [37], the bulk velocity is a better assumption for the convection velocity of the vortex sheet than the velocity at the vena contracta or half of it as suggested by Howe [8]. The average convection velocities found for the medium hole are 80% of the bulk velocity for σ_1 and 63% of the bulk velocity for σ_2 . A lower convection velocity for σ_2 than for σ_1 is expected since σ_1 is located inside the jet of the hole where the mean flow velocities are higher. A lower convection velocity for σ_1 than in the short hole case is also to be expected since the flow reattaches in the medium hole leading to lower mean flow velocities in the second half of the hole.

Guzmán-Iñigo et al. [37] studied the influence of the vortex sheet convection velocity on the acoustic response predicted by a similar model for short holes. They reported that the convection velocity does not change the peak values of the Rayleigh conductivity but the Strouhal number at which these peaks occur. However, in the situation where the two vortex sheets σ_1 and σ_2 interact, the choice of different convection velocities translate to a phase shift between the vortical structures of the individual sheets and can therefore influence the trends of the predicted impedance.

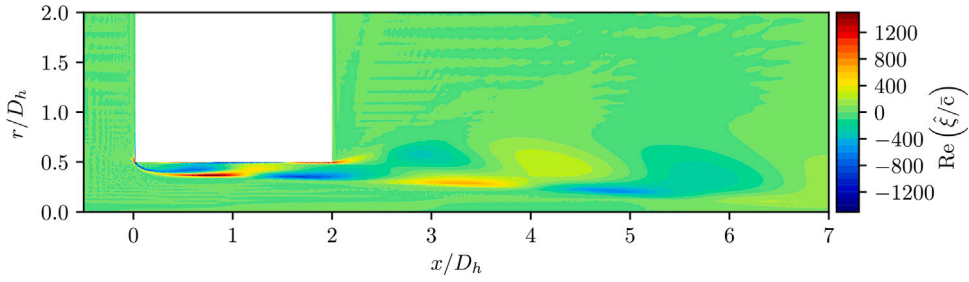


Fig. 8. Real part of normalised perturbation vorticity at $St = 0.82$. Minima and maxima of vortex structures along a vortex sheet are connected.

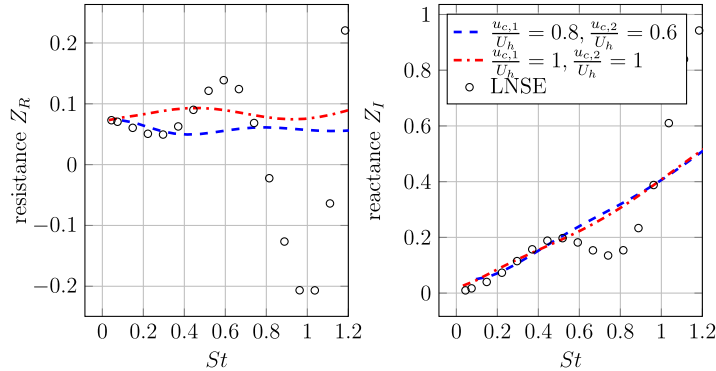


Fig. 9. Normalised impedance Z for a hole with $L_h/D_h = 2.0$ obtained with the vortex sheet model including both vortex sheets for different convection velocities. Results are compared with the LNSE data.

Fig. 9 shows that the choice of the correct convection velocities allows the model to predict the LNSE trends for resistance and reactance in the low Strouhal number regime up to $St < 0.4$ with good quantitative agreement. At higher frequencies, however, the model does not reproduce the trends predicted by the simulations.

4.4.2. Strength variation of vortex sheets

The results presented in Fig. 9 show that tuning of the convection velocities alone is not sufficient to achieve a quantitative match between model prediction and LNSE for higher Strouhal numbers $St \gtrsim 0.4$. The physical mechanism allowing the medium hole to whistle is so far missed in the acoustic modelling. The vortex-sound models assume a constant vortex sheet strength σ along the vortex sheet path that is determined by the Kutta condition at the shedding point. However, the strength of the vorticity will, in reality, grow/decay due to shear-layer instabilities [45] and dissipation by turbulence. This variation of the vorticity strength while being convected has not been considered so far by any vortex-sound model. In this section, we analyse this effect and incorporate it to the model.

Fig. 10 shows the radial distribution of the normalised perturbation vorticity at different positions x/D_h along the hole axis for $St = 0.82$. As observed in Fig. 5, the strong gradients of the flow variables at the inlet preclude an accurate computation of the vorticity field there. For this reason, the position $x/D_h = 0.2$ is selected to represent the vorticity shed at the inlet edge. At the hole outlet, $x/D_h = 2.0$, one vorticity peak at $r/D_h \approx 0.35$ corresponding to the vortex sheet shed from the inlet edge σ_1 is observed. High vorticity is also found close to the wall—in the acoustic boundary layer. Downstream of the hole at $x/D_h = 3.0$, two vorticity peaks relating to the shed vorticity from the inlet edge at $r/D_h \approx 0.3$ and outlet edge at $r/D_h \approx 0.55$ can be clearly identified.

The cross-sectional average vorticity for a given vortex sheet can be computed as

$$\sigma_i(x) = \frac{\int_{A_i} \tilde{\xi}(x) dA}{A_i} = \frac{2 \int_{R_{0,i}}^{R_{f,i}} \tilde{\xi}(x) r dr}{(R_{f,i}^2 - R_{0,i}^2)}, \tag{22}$$

where $A_i(x)$ is the cross-sectional area where a given vortex sheet is defined, and $R_{0,i}$ and $R_{f,i}$ the radial positions bounding that area. For the vortex sheet shed at the inlet edge, σ_1 , Eq. (22) is integrated from the hole axis to $R_{f,1}/D_h = 0.49$ so that the vorticity at the boundary layer is excluded. For the vorticity shed at the downstream edge, σ_2 , the limits of integration extend from $R_{0,2}/D_h = 0.49$ to $R_{f,2}/D_h = 1.0$.

The strengths of the vortex sheets convected from the inlet edge σ_1 and outlet edge σ_2 along the hole axis are plotted in Fig. 11. For $St = 0.3$, σ_1 increases up to the middle of the hole ($x/D_h = 1.0$) due to an instability of the shear layer [45]. For $x/D_h > 1.0$, the turbulent dissipation of vorticity dominates. Note that the reattachment of the mean flow in Fig. 1(b) at $x/D_h = 1.22$ also indicates

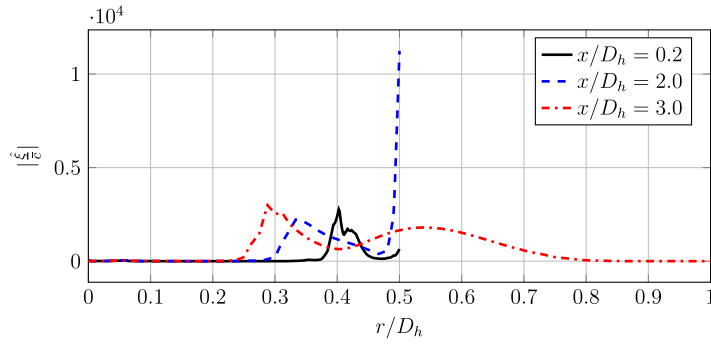


Fig. 10. Radial distribution of the normalised perturbation vorticity at different positions x/D_h along the hole axis for $St = 0.82$.

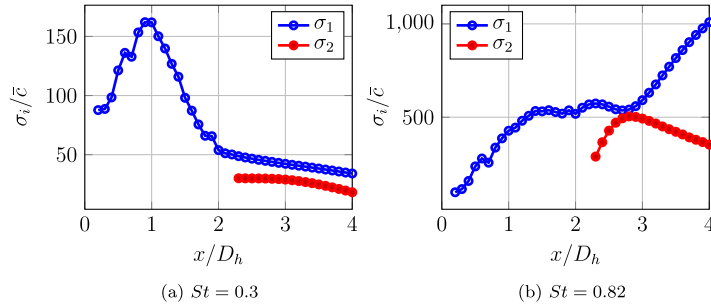


Fig. 11. Normalised strengths of vortex sheets shed from the hole inlet at $x/D_h = 0.0$ (σ_1) and outlet at $x/D_h = 2.0$ (σ_2).

strong turbulence in this region. Downstream of the hole, σ_1 and σ_2 are dissipated. For $St = 0.82$, σ_1 increases in the first half of the hole. In the second half of the hole, the vortex sheet strength stays constant at $\sigma_1 \approx 700$. Downstream of the hole, σ_1 is further amplified. The vortex sheet σ_2 is amplified downstream of the hole and reaches a maximum of $\sigma_2 \approx 500$ at $x/D_h \approx 3.0$. For $x/D_h \gtrsim 3.0$ it is dissipated.

Looking at Fig. 11, the assumption used for short holes [9,17] that the vortex sheet strength is constant is justified since it does not significantly change for $x/D_h < 0.5$. Thus, for short holes, the vortex sheet is convected out of the hole before the vorticity is significantly increased. In contrast, for medium holes, the strength of σ_1 at the shedding point can significantly differ from the strength at the hole outlet plane depending on the Strouhal number. To include this effect in the semi-analytical model, the growth ratio

$$\sigma_r = \frac{|\sigma_{1,\text{outlet}}|}{|\sigma_{1,\text{inlet}}|} \tag{23}$$

between the vorticity at the hole outlet plane $\sigma_{1,\text{outlet}}$ and shedding point $\sigma_{1,\text{inlet}}$ is introduced. The vortex sheet strength inside the hole is then set to $\sigma_1 = \sigma_{1,\text{inlet}}$, which is determined by the Kutta condition, and jumps to $\sigma_1 = \sigma_r \sigma_{1,\text{inlet}}$ at the hole outlet plane as shown in Fig. 6. Note that σ_r is an additional model parameter and needs to be defined a priori. The idea of modelling the vortex sheet strength with a jump function – instead of a continuous distribution along the hole – is motivated by the fact that most of the scattering of vorticity into acoustics takes places in the vicinity of the hole edges [46].

Fig. 12 compares the normalised impedance predicted with the vortex-sound model including σ_1 and σ_2 for different growth ratios σ_r . The convection velocities of σ_1 and σ_2 are set according to the LNSE results to $u_{c,1}/\bar{c} = 0.8Ma_h$ and $u_{c,2}/\bar{c} = 0.6Ma_h$, respectively. From the investigated growth ratios, $\sigma_r = 1$ gives the best quantitative match between the prediction of the vortex sheet model for the resistance and reactance and the LNSE results at low Strouhal numbers up to $St < 0.4$. Yet the trends at higher Strouhal numbers are not captured. By increasing the growth ratio in the semi-analytical model to $\sigma_r = 3$ and $\sigma_r = 5$, the maximum and minimum in resistance predicted by the LNSE at $St \approx 0.6$ and $St \approx 1.0$ are captured. The same holds for the maximum and minimum in reactance at $St \approx 0.4$ and $St \approx 0.7$. If the growth ratio is further increased to $\sigma_r = 9$ and $\sigma_r = 13$, the predicted resistance becomes negative at $0.8 < St < 1.2$ and the model predicts successfully the whistling of medium holes in the high Strouhal number regime.

The variation of the vorticity growth factor with the Strouhal number in the LNSE is given in Fig. 13. To compute this plot, the vortex sheet strength at the inlet was extrapolated from the vortex sheet strengths at positions $x/D_h = 0.2$ and $x/D_h = 0.3$. Following Fig. 13, the growth ratio at $St = 0.3$ is $\sigma_r \approx 0.63$ and at $St = 0.82$ is $\sigma_r \approx 8.1$, indicating that $\sigma_r > 1$ should be chosen for higher Strouhal numbers.

Fig. 14 shows a blend of the independent plots in Fig. 12 for a Strouhal-number-dependent growth factor according to Fig. 13. The model predictions clearly follow the LNSE results for all the frequencies investigated. The quantitative differences between

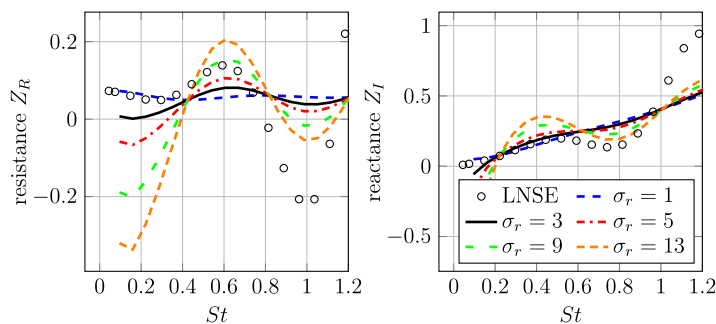


Fig. 12. Normalised impedance Z for a hole with $L_h/D_h = 2.0$ obtained with the vortex sheet model for different growth ratios σ_r . Results are compared with the LNSE data.

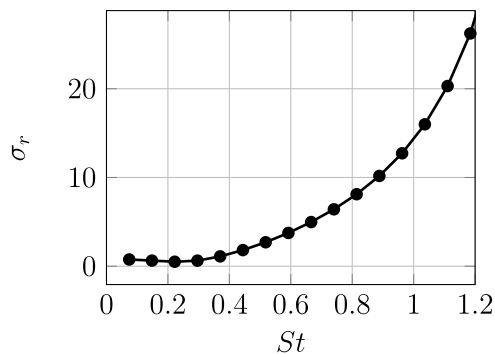


Fig. 13. Vorticity growth rate in dependence of the Strouhal number.

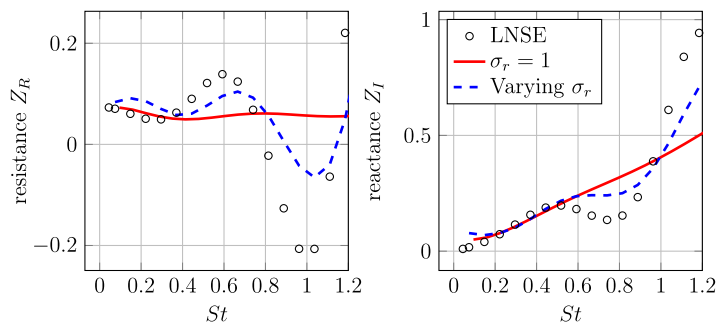


Fig. 14. Normalised impedance Z for a hole with $L_h/D_h = 2.0$ obtained with the vortex sheet model with varying growth factor according to Fig. 13.

LNSE and model are most likely due to the LNSE being not able to give exact quantitative values for the vorticity growth inside the hole but more the general trends. For example, uncertainty is introduced by the turbulence modelling and post processing of the vortex sheet strength. Furthermore, modelling the shear layer instability with a discrete jump in vortex sheet strength is a crude approximation. A better prediction may be achieved by using a continuously varying vortex strength along the vortex sheet path. However, this would require more input parameters to the model. Nevertheless, the chosen modelling approach positively indicates that the vorticity growth inside the hole is an important mechanism for the acoustics of medium holes.

5. Conclusions

The present paper provides a numerical and theoretical study of the acoustics of holes with length-to-diameter ratios of $1.5 < L_h/D_h < 3$, and thus falling in the border region between conventional short [7,18–21] and long holes [20,21]. The numerical approach is based on a linearisation of the Navier–Stokes equations around a turbulent mean flow [27–29]. The mean flow was computed as a solution of the RANS equations. The linearised equations were recast in the frequency domain and solved using a

finite element method. This approach, usually referred as two-step approach, is limited to configurations (length-to-diameter ratios) where a steady mean flow exists.

From the numerical study, holes with length-to-diameter ratios between $1.5 < L_h/D_h < 3$ were found to be able to whistle in an approximately three-times-higher Strouhal number regime than short holes, i.e. $0.75 < St < 1.1$ (compared to $0.2 < St < 0.35$ for short holes). If the Strouhal number is based on the hole length, the whistling regime of these holes collapse, leading to our definition of medium holes: medium holes are long in the sense that the mean flow reattaches inside them [11–13] but differ from conventional long holes by their whistling ability. By incorporating flow features from the LNSE results into semi-analytical vortex-sound models [9,17,32], the three-way coupling between two vortex sheets shed from the inlet and outlet edges of the hole with the acoustic field, as well as the amplification of vorticity inside the hole, were identified as the main physical mechanisms to explain the acoustic behaviour of such medium holes.

For technical applications, these results show that holes with length-to-diameter ratios of $1.5 < L_h/D_h < 3.0$ sustaining a bias flow should be applied with care since they can introduce acoustical energy into noise-controlling systems at relatively high Strouhal numbers. For example, recent experimental studies of thermo-acoustic instabilities in a cryogenic rocket engine show that a global instability of the rocket could be induced by the whistling of a hole with $L_h/D_h = 1.5$ located at the head of the liquid oxygen injector [1,2].

Although experimental evidence of the whistling of medium holes exists [19,23], detailed impedance measurements for $St > 0.4$ for this class of holes were not found in the literature. With increasing frequency, the acoustic length scales become smaller and stronger spatial gradients of the perturbation velocity, i.e. higher strain rates, are the consequences. This leads to an increased influence of the eddy viscosity at higher frequencies so that the turbulence modelling [30,31] will influence foremost the high Strouhal number regime of the solution. An experimental study of the impedance of medium holes at higher Strouhal numbers would be therefore of interest to confirm the findings obtained in this publication for high Strouhal numbers.

Since the shear layer stability inside the hole seems to be crucial for the whistling mechanism of medium holes, a detailed hydrodynamic stability analysis can be the scope of further work to understand the physical mechanism in more detail.

CRediT authorship contribution statement

Philipp Brokof: Methodology, Investigation, Writing – original draft. **Juan Guzmán-Iñigo:** Conceptualization, Methodology, Software, Writing – review & editing. **Dong Yang:** Resources, Methodology. **Aimee S. Morgans:** Funding acquisition, Supervision.

Declaration of competing interest

The authors declare that they have no known competing financial interests or personal relationships that could have appeared to influence the work reported in this paper.

Data availability

Data will be made available on request.

Acknowledgements

The authors would like to gratefully acknowledge the support of the Erasmus+ program of the European Union and the ERC Consolidator Grant AFIRMATIVE (2018–23).

Appendix A. Impedance for short holes

Fig. A.1 shows the real Z_R and imaginary part Z_I of the normalised impedance as defined in Eq. (3) for a hole with $L_h/D_h = 0.5$. The LNSE results reproduce the experimental data for the resistance and the match improves with increasing expansion ratio $\lambda = D_d/D_h = D_u/D_h$ between hole and ducts. The reactance follows the experimental trend but is under-predicted by the LNSE simulations. This is most likely due to differences in the setup, e.g. the flow exits to a plenum in experiments but a circular duct is arranged downstream of the hole in the simulations and multiple holes are present in experiment.

In Fig. A.2 the LNSE results are compared with experimental data from [26]. In this experiment, a single hole is tested and the downstream part is well defined by a circular duct with expansion ratio $\lambda_d = 2$. For this well defined case, the agreement of the LNSE results with the experiment is excellent.

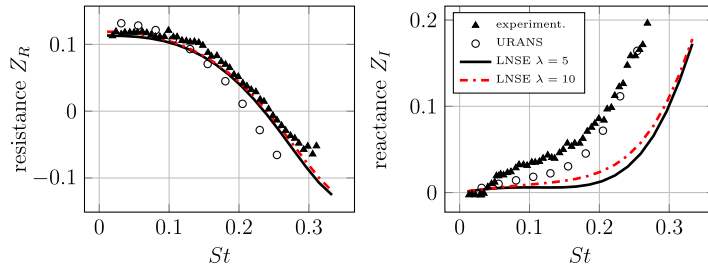


Fig. A.1. Normalised impedance Z for a hole with $L_n/D_n = 0.5$ for different expansion ratios λ . Comparison with experimental data [21] and CFD results [20].

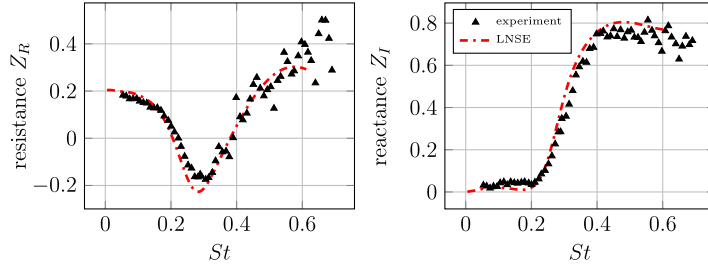


Fig. A.2. Normalised impedance Z for a hole with $L_n/D_n = 0.3$. Comparison with experimental data from [26].

Appendix B. Anechoic and forcing acoustic boundary conditions

Eqs. (8) and (9) are discretised with ansatz functions

$$\hat{\rho}^h, \hat{u}_i^h \in S^h \subset S = \{v \in H^1(\Omega) : v = u_D \text{ on } \Gamma_D\}. \quad (B.1)$$

The weak formulations are obtained by multiplication with test functions, chosen from the trial function space so that

$$w_\rho^h, w_{u,i}^h \in \mathcal{V}^h \subset \mathcal{V} = \{v \in H^1(\Omega) : v = 0 \text{ on } \Gamma_D\}, \quad (B.2)$$

and integration over the domain Ω with Dirichlet Γ_D and Neumann Γ_N boundaries. In the following, the superscript h for discrete approximations is dropped for the sake of readability and L2-inner products on Ω and Γ_N are denoted with $(f, g)_\Omega$ and $(f, g)_{\Gamma_N}$, respectively. The finite element formulation is stabilised by a least-squares stabilisation [47], employing the residual operators

$$R_c(\hat{\rho}, \hat{\mathbf{u}}) = i\omega\hat{\rho} + \nabla \cdot (\hat{\rho}\hat{\mathbf{u}} + \hat{\rho}\hat{\mathbf{u}}) = 0, \quad (B.3)$$

$$R_m(\hat{\rho}, \hat{\mathbf{u}}) = i\omega\hat{\rho}\hat{\mathbf{u}} + (\hat{\rho}\hat{\mathbf{u}} + \hat{\rho}\hat{\mathbf{u}}) \cdot \nabla\hat{\mathbf{u}} + \nabla \cdot \left(\hat{\rho}\underline{\underline{\mathbf{I}}} - \hat{\underline{\underline{\tau}}}^{\text{tot}} \right) = 0. \quad (B.4)$$

This leads to the stabilised weak formulation in frequency domain as

$$\begin{aligned} (w_\rho, i\omega\hat{\rho})_\Omega + (w_\rho, \nabla \cdot (\hat{\rho}\hat{\mathbf{u}} + \hat{\rho}\hat{\mathbf{u}}))_\Omega \\ + (R_c(w_\rho, \mathbf{w}_u)\tau_\rho, R_c(\hat{\rho}, \hat{\mathbf{u}}))_\Omega = 0, \quad \forall w_\rho, \mathbf{w}_u \in \mathcal{V}^h, \end{aligned} \quad (B.5)$$

$$\begin{aligned} (\mathbf{w}_u, i\omega\hat{\rho}\hat{\mathbf{u}})_\Omega + (\mathbf{w}_u, (\hat{\rho}\hat{\mathbf{u}} + \hat{\rho}\hat{\mathbf{u}}) \cdot \nabla\hat{\mathbf{u}})_\Omega \\ + (\mathbf{w}_u, \nabla \cdot \left(\hat{\rho}\underline{\underline{\mathbf{I}}} - \hat{\underline{\underline{\tau}}}^{\text{tot}} \right))_\Omega \\ + (R_m(w_\rho, \mathbf{w}_u)\tau_u, R_m(\hat{\rho}, \hat{\mathbf{u}}))_\Omega = 0, \quad \forall w_\rho, \mathbf{w}_u \in \mathcal{V}^h. \end{aligned} \quad (B.6)$$

By applying the Gauss' theorem and integration by parts, mass fluxes \mathbf{h}_c and momentum fluxes $\underline{\underline{\mathbf{h}}}_m$ over the domain boundary can be naturally introduced in the weak formulation:

$$(w_\rho, \nabla \cdot (\hat{\rho}\hat{\mathbf{u}} + \hat{\rho}\hat{\mathbf{u}}))_\Omega = (w_\rho, \mathbf{h}_c)_{\Gamma_N} - (\hat{\rho}\hat{\mathbf{u}} + \hat{\rho}\hat{\mathbf{u}}, \nabla w_\rho)_\Omega, \quad (B.7)$$

$$(\mathbf{w}_u, \nabla \cdot \left(\hat{\rho}\underline{\underline{\mathbf{I}}} - \hat{\underline{\underline{\tau}}}^{\text{tot}} \right))_\Omega = (\mathbf{w}_u, \underline{\underline{\mathbf{h}}}_m)_{\Gamma_N} - \left(\left(\hat{\rho}\underline{\underline{\mathbf{I}}} - \hat{\underline{\underline{\tau}}}^{\text{tot}} \right), \nabla \mathbf{w}_u \right)_\Omega. \quad (B.8)$$

This naturally allows to impose an anechoic boundary condition by applying flux vector splitting [48] at the boundary and only incorporating outgoing fluxes in the weak formulation. In Fig. 2, fluxes across the domain inlet (Γ_{in}) and outlet (Γ_{out}) are foremost in axial direction. If the influence of viscosity is assumed to be restricted to the boundary layers at the walls Γ_u and Γ_d , the flow

behaves mostly inviscid at the inlet and outlet and the flux vector can be formulated as

$$\hat{\mathbf{F}} = \begin{pmatrix} \bar{\rho}\hat{u}_x + \bar{\rho}\hat{u}_x \\ \bar{u}_x\bar{\rho}\hat{u}_x + \hat{p} \\ \bar{\rho}\hat{u}_x\hat{u}_y \end{pmatrix} = \begin{pmatrix} h_{e,x} \\ h_{m,xx} \\ h_{m,xy} \end{pmatrix}. \tag{B.9}$$

For the linearised Euler equations, the flux vector can be written as the matrix product of the Jacobian $\hat{\underline{\underline{A}}}_x$ and the vector of conserved flow variables $\hat{\mathbf{U}} = (\hat{p}, \bar{\rho}\hat{u}_x, \bar{\rho}\hat{u}_y)^T$,

$$\hat{\mathbf{F}} = \hat{\underline{\underline{A}}}_x \hat{\mathbf{U}}. \tag{B.10}$$

The eigenvalues of the Jacobian are then $\hat{\lambda}_k = (\bar{u}_x, \bar{u}_x + \bar{c}, \bar{u}_x - \bar{c})$ with \bar{c} as the speed of sound of the mean flow. Using the linear transformation $\hat{\underline{\underline{V}}} = (\hat{v}_1, \hat{v}_2, \hat{v}_3)$ consisting of the corresponding eigenvectors of $\hat{\underline{\underline{A}}}_x$, the Riemann invariants $\hat{\mathbf{W}}$ of the PDE system [49] can be obtained as

$$\hat{\mathbf{W}} = \hat{\underline{\underline{V}}}^{-1} \hat{\mathbf{U}} = \begin{pmatrix} \bar{\rho}\hat{u}_y \\ \frac{\bar{\rho}\hat{u}_x}{2} + \frac{\hat{p}\bar{c}}{2} \\ \frac{\bar{\rho}\hat{u}_x}{2} - \frac{\hat{p}\bar{c}}{2} \end{pmatrix}. \tag{B.11}$$

The outgoing fluxes for the anechoic boundary formulation can then be obtained as

$$\hat{\mathbf{F}}_{\text{inlet,out}} = \hat{\underline{\underline{V}}}_x^- \hat{\mathbf{W}}, \quad \hat{\mathbf{F}}_{\text{outlet,out}} = \hat{\underline{\underline{V}}}_x^+ \hat{\mathbf{W}}, \tag{B.12}$$

where the matrices $\hat{\underline{\underline{V}}}_x^+$ and $\hat{\underline{\underline{V}}}_x^-$ contain only positive or negative eigenvalues that are correlated to information transport in and opposite to the mean flow direction, respectively.

The flux vector splitting approach introduced for anechoic boundaries naturally allows to force the flow acoustically. The incoming fluxes at the inlet Γ_{in} is

$$\hat{\mathbf{F}}_{\text{inlet,in}} = \hat{\underline{\underline{V}}}_x^+ \hat{\mathbf{W}} = \begin{pmatrix} \frac{\bar{u}_x + \bar{c}}{\bar{c}} \left(\frac{\hat{p}\bar{c}}{2} + \frac{\bar{\rho}\hat{u}_x}{2} \right) \\ (\bar{u}_x + \bar{c}) \left(\frac{\hat{p}\bar{c}}{2} + \frac{\bar{\rho}\hat{u}_x}{2} \right) \\ \bar{u}_x \bar{\rho} \hat{u}_y \end{pmatrix} = \begin{pmatrix} \frac{\bar{u}_x + \bar{c}}{\bar{c}} \hat{f} \\ (\bar{u}_x + \bar{c}) \hat{f} \\ \bar{u}_x \bar{\rho} \hat{u}_y \end{pmatrix}. \tag{B.13}$$

Comparison with Eq. (B.11) shows that the incoming flux vector contains the Riemann invariant $\hat{f} = \left(\frac{\hat{p}\bar{c}}{2} + \frac{\bar{\rho}\hat{u}_x}{2} \right)$ with the physical meaning of a one-dimensional planar wave entering the domain [29]. By including the incoming flux at the inlet in the weak formulation and setting $\hat{f} = a + ib$, a forcing of amplitude $\sqrt{a^2 + b^2}$ and phase difference $\tan(b/a)$ is prescribed. Since planar waves in x -direction are predominant, at Γ_{in} and Γ_{out} in Fig. 2, $\hat{u}_y = 0$ is assumed in Eq. (B.13).

References

- [1] W. Armbruster, J.S. Hardi, D. Suslov, M. Oswald, Injector-driven flame dynamics in a high-pressure multi-element oxygen-hydrogen rocket thrust chamber, *J. Propuls. Power* 35 (3) (2019) 632–644, <http://dx.doi.org/10.2514/1.B37406>.
- [2] S. Gröning, J.S. Hardi, D. Suslov, M. Oswald, Injector-driven combustion instabilities in a hydrogen/oxygen rocket combustor, *J. Propuls. Power* 32 (3) (2016) 560–573, <http://dx.doi.org/10.2514/1.B35768>.
- [3] X. Jing, X. Sun, Experimental investigations of perforated liners with bias flow, *J. Acoust. Soc. Am.* 106 (5) (1999) 2436–2441, <http://dx.doi.org/10.1121/1.428128>.
- [4] V. Bellucci, P. Flohr, C.O. Paschereit, F. Magni, On the use of Helmholtz resonators for damping acoustic pulsations in industrial gas turbines, *J. Eng. Gas Turbines and Power* 126 (2) (2004) 271–275, <http://dx.doi.org/10.1115/1.1473152>.
- [5] E. Boujo, C. Bourquard, Y. Xiong, N. Noiray, Processing time-series data of randomly forced self-oscillators: The example of beer bottle whistling, *J. Sound Vib.* 464 (2020) 114981, <http://dx.doi.org/10.1016/j.jsv.2019.114981>.
- [6] X. Jing, X. Sun, Effect of plate thickness on impedance of perforated plates with bias flow, *AIAA J.* 38 (9) (2000) 1573–1578, <http://dx.doi.org/10.2514/2.1139>.
- [7] R. Lacombe, Y. Aurégan, P. Moussou, Whistling of an orifice in a reverberating duct at low Mach number, *J. Acoust. Soc. Am.* 130 (2011) 2662–2667, <http://dx.doi.org/10.1121/1.3641427>.
- [8] M.S. Howe, On the theory of unsteady high Reynolds number flow through a circular aperture, *Proc. R. Soc. London. A. Math. Phys. Sci.* 366 (1725) (1979) 205–223, <http://dx.doi.org/10.1098/rspa.1979.0048>.
- [9] D. Yang, A.S. Morgans, A semi-analytical model for the acoustic impedance of finite length circular holes with mean flow, *J. Sound Vib.* 384 (2016) 294–311, <http://dx.doi.org/10.1016/j.jsv.2016.08.006>.
- [10] S. Pope, *Turbulent Flows*, Cambridge University Press, Cambridge, ISBN: 9780521598866, 2000.
- [11] A. Lichtarowicz, R.K. Duggins, E. Markland, Discharge coefficients for incompressible non-cavitating flow through long orifices, *J. Mech. Eng. Sci.* 7 (2) (1965) 210–219, http://dx.doi.org/10.1243/JMES_JOUR_1965_007_029_02.
- [12] N. Hay, A. Spencer, Discharge coefficients of cooling holes with radiused and chamfered inlets, *J. Turbomach.* 114 (4) (1992) 701–706, <http://dx.doi.org/10.1115/1.2928022>.
- [13] I.E. Idelchik, *Handbook of Hydraulic Resistance*, fourth ed., Begell House, ISBN: 9781567002515, 2007.
- [14] P.A. Kolodize Jr., M. Van Winkle, Discharge coefficients through perforated plates, *AIChE J.* 3 (3) (1957) 305–312, <http://dx.doi.org/10.1002/aic.690030304>.
- [15] D.C. Rennels, H.M. Hudson, *Pipe Flow: A Practical and Comprehensive Guide*, John Wiley & Sons, 2012.
- [16] M.S. Howe, *Theory of Vortex Sound*, Cambridge University Press, ISBN: 9780521012232, 2002.

- [17] D. Yang, A.S. Morgans, The acoustics of short circular holes opening to confined and unconfined spaces, *J. Sound Vib.* 393 (2017) 41–61, <http://dx.doi.org/10.1016/j.jsv.2016.12.027>.
- [18] P. Testud, P. Mossou, A. Hirschberg, Y. Aurégan, Noise generated by cavitating single-hole and multi-hole orifices in a water pipe, *J. Fluid Struct.* 23 (2) (2007) 163–189, <http://dx.doi.org/10.1016/j.jfluidstruct.2006.08.010>.
- [19] P. Moussou, P. Testud, Y. Aurégan, A. Hirschberg, An acoustic criterion for the whistling of orifices in pipes, in: *ASME Pressure Vessels and Piping Conference 22 To 26 July 2007*, ASME, San Antonio, Texas, 2009, pp. 345–353, <http://dx.doi.org/10.1115/PVP2007-26157>.
- [20] J. Su, J. Rupp, A. Garmory, J.F. Carotte, Measurements and computational fluid dynamics predictions of the acoustic impedance of orifices, *J. Sound Vib.* 352 (2015) 174–191, <http://dx.doi.org/10.1016/j.jsv.2015.05.009>.
- [21] J. Rupp, *Acoustic Absorption and the Unsteady Flow Associated with Circular Apertures in a Gas Turbine Environment* (Ph.D. thesis), Loughborough University, 2013.
- [22] Z. Chen, Z. Ji, H. Huang, Acoustic impedance of perforated plates in the presence of bias flow, *J. Sound Vib.* 446 (2019) 159–175, <http://dx.doi.org/10.1016/j.jsv.2019.01.031>.
- [23] P. Testud, *Aéro-acoustique des Diaphragmes En Conduit: Sifflement et Cavitation* (Ph.D. thesis), Académie de Nantes, 2006.
- [24] S. Föller, W. Polifke, Identification of aero-acoustic scattering matrices from large eddy simulation. Application to a sudden area expansion of a duct, *J. Sound Vib.* 331 (13) (2012) 3096–3113, <http://dx.doi.org/10.1016/j.jsv.2012.01.004>.
- [25] R. Lacombe, S. Föller, G. Jasor, W. Polifke, Y. Aurégan, P. Moussou, Identification of aero-acoustic scattering matrices from large eddy simulation: Application to whistling orifices in duct, *J. Sound Vib.* 332 (20) (2013) 5059–5067, <http://dx.doi.org/10.1016/j.jsv.2013.04.036>.
- [26] R. Lacombe, P. Moussou, Y. Aurégan, Identification of whistling ability of a single hole orifice from an incompressible flow simulation, in: *Pressure Vessels and Piping Conference, Volume 4: Fluid-Structure Interaction*, 2011, pp. 261–267, <http://dx.doi.org/10.1115/PVP2011-57355>.
- [27] A. Kierkegaard, S. Boij, G. Efraimsson, A frequency domain linearized Navier-Stokes equations approach to acoustic propagation in flow ducts with sharp edges, *J. Acoust. Soc. Am.* 2 (127) (2010) 710–719, <http://dx.doi.org/10.1121/1.3273899>.
- [28] A. Kierkegaard, S. Boij, G. Efraimsson, Simulations of the scattering of sound waves at a sudden area expansion, *J. Sound Vib.* 331 (5) (2012) 1068–1083, <http://dx.doi.org/10.1016/j.jsv.2011.09.011>.
- [29] J. Gikadi, M. Schulze, J. Schwing, S. Föller, T. Sattelmayer, Linearized Navier-Stokes and Euler equations for the determination of the acoustic scattering behaviour of an area expansion, in: *18th AIAA/CEAS Aeroacoustics Conference 04 to 06 June 2012*, AIAA, Colorado Springs, 2012, <http://dx.doi.org/10.2514/6.2012-2292>.
- [30] J. Gikadi, S. Föller, T. Sattelmayer, Impact of turbulence on the prediction of linear aeroacoustic interactions: Acoustic response of a turbulent shear layer, *J. Sound Vib.* 333 (24) (2014) 6548–6559, <http://dx.doi.org/10.1016/j.jsv.2014.06.033>.
- [31] A. Holmberg, A. Kierkegaard, C. Weng, A frequency domain linearized Navier-Stokes method including acoustic damping by eddy viscosity using RANS, *J. Sound Vib.* 346 (2015) 229–247, <http://dx.doi.org/10.1016/j.jsv.2015.02.030>.
- [32] J. Su, D. Yang, A.S. Morgans, Modelling of sound-vortex interaction for the flow through an annular aperture, *J. Sound Vib.* 509 (2021) 116250, <http://dx.doi.org/10.1016/j.jsv.2021.116250>.
- [33] D. Fabre, R. Longobardi, P. Bonnefils, P. Luchini, The acoustic impedance of a laminar viscous jet through a thin circular aperture, *J. Fluid Mech.* 864 (2019) 5–44, <http://dx.doi.org/10.1017/jfm.2018.1008>.
- [34] A.K.M.F. Hussain, W.C. Reynolds, The mechanics of organized wave in turbulent shear flow, *J. Fluid Mech.* 41 (2) (1970) 241–258, <http://dx.doi.org/10.1017/S0022112070000605>.
- [35] H.G. Weller, G. Tabor, H. Jasak, C. Fureby, A tensorial approach to computational continuum mechanics using object-orientated techniques, *Comput. Phys.* 12 (1998) 620–631, <http://dx.doi.org/10.1063/1.168744>.
- [36] F.R. Menter, M. Knutz, R. Langtry, Ten years of industrial experience with the SST turbulence model, in: *4th International Symposium Turbulence, Heat and Mass Transfer 2003*, Begell House, Inc., Antalya, Turkey, ISBN: 1567001963, 2003.
- [37] J. Guzmán-Iñigo, D. Yang, H.G. Johnson, A.S. Morgans, Sensitivity of the acoustics of short circular holes with bias flow to inlet edge geometries, *AIAA J.* 57 (11) (2019) 4835–4844, <http://dx.doi.org/10.2514/1.J057996>.
- [38] D.C. Wilcox, *Turbulence Modeling for CFD*, third ed., DCW Industries, La Cañada, Calif, ISBN: 1928729088, 2006.
- [39] J. Guzmán-Iñigo, D. Yang, R. Gaudron, A.S. Morgans, On the scattering of entropy waves at sudden area expansions, *J. Sound Vib.* 540 (2022) 117261, <http://dx.doi.org/10.1016/j.jsv.2022.117261>.
- [40] M. Alnæs, J. Blechta, J. Hake, A. Johansson, B. Kehlet, A. Logg, C. Richardson, J. Ring, M.E. Rognes, G.N. Wells, The FEniCS project version 1.5, *Arch. Numer. Software* 3 (100) (2015) 9–23, <http://dx.doi.org/10.11588/ans.2015.100.20553>.
- [41] S.-H. Jang, J.-G. Ih, On the multiple microphone method for measuring in-duct acoustic properties in the presence of mean flow, *J. Acoust. Soc. Am.* 103 (3) (1998) <http://dx.doi.org/10.1121/1.421289>.
- [42] T. Pedergrana, C. Bourquard, A. Faure-Beaulieu, N. Noiray, Modeling the nonlinear aeroacoustic response of a harmonically forced side branch aperture under turbulent grazing flow, *Phys. Rev. Fluids* 6 (2) (2021) 023903, <http://dx.doi.org/10.1103/PhysRevFluids.6.023903>.
- [43] M. Son, W. Armbruster, F. Tonti, J. Hardi, Numerical study of acoustic resonance in a LOX injector post induced by orifice flow, in: *AIAA Propulsion and Energy Forum August 9 to August 11 2021*, AIAA, Virtual Event, 2021, <http://dx.doi.org/10.2514/6.2021-3568>.
- [44] B.E.L. Deckker, Y.F. Chang, Paper 7: An investigation of steady compressible flow through thick orifices, in: *Proceedings of the Institution of Mechanical Engineers, Conference Proceedings*, vol. 180, (no. 10) Sage Publications Sage UK: London, England, 1965, pp. 312–323, http://dx.doi.org/10.1243/PIME_CONF_1965_180_307_02.
- [45] P.-J. Schmid, D.S. Henningson, *Stability and Transition in Shear Flows*, Springer Verlag, New York, ISBN: 9780387989853, 2000.
- [46] R.M. Schleicher, M.S. Howe, On the interaction of sound with an annular aperture in a mean flow duct, *J. Sound Vib.* 332 (2013) 5594–5605, <http://dx.doi.org/10.1016/j.jsv.2013.05.006>.
- [47] J. Donea, A. Huerta, *Finite Element Methods for Flow Problems*, John Wiley & Sons, Ltd., West Sussex, ISBN: 0471496669, 2003.
- [48] J.L. Steger, R.F. Warming, Flux vector splitting of the inviscid gasdynamic equations with application to finite-difference methods, *J. Comput. Phys.* 40 (2) (1981) 263–293, [http://dx.doi.org/10.1016/0021-9991\(81\)90210-2](http://dx.doi.org/10.1016/0021-9991(81)90210-2).
- [49] R.J. LeVeque, *Finite Volume Methods for Hyperbolic Problems*, Cambridge University Press, Cambridge, ISBN: 9780521009249, 2002.